European volcanological supersite in Iceland: a monitoring system and network for the future

Report

D5.6 - Velocity model and seismicity associated with melt movement

Work Package:	*Long term magma tracking*
Work Package number:	*5*
Deliverable:	*Velocity model and seismicity associated with melt movement*
Deliverable number:	*5.6*
Type of Activity:	*RTD*
Responsible activity leader:	*Andy Hooper*
Responsible participant:	*University of Cambridge*
Authors:	*Robert White (Cambridge), Robert Green (Cambridge)*

Type of Deliverable:	*Report*	*[X]*	*Demonstrator*	*[ ]*
	Prototype	*[ ]*	*Other*	*[ ]*
Dissemination level:	*Public*	*[X]*	*Restricted Designated Group*	*[ ]*
	Prog. Participants (FP7)	*[ ]*	*Confidential (consortium)*	*[ ]*

Seventh Framework Programme
EC project number: 308377

Abstract

Cambridge University were responsible for developing a 3D velocity model beneath central Iceland and for using seismological methods to track underground magma movement. We have used essentially the same array of seismometers for both tasks. FutureVolc funded the deployment of 8 broad-band seismometers around Vatnajökull primarily for the development of the 3D velocity model which requires low frequency ambient noise data. These seismometers were supplemented by 67 other Cambridge seismometers deployed with other funds, and by seismometers from the Icelandic Meteorological Office. We also historic seismic data from earlier deployments in Iceland for building a comprehensive velocity model. The magma tracking used mainly higher frequency (c. 8 Hz) data, although some low-frequency tremor was recorded.

This work has produced the best constrained to date regional crustal 3D velocity model of Iceland which in combination with results from seismic refraction profiles and receiver function analysis will be of use for future seismic monitoring and understanding of the crustal structure under Iceland. The 2014-15 Bardarbunga – Holuhraun eruption provided a spectacular example of 46 km long lateral flow of melt along a dyke prior to eruption, which by virtue of the large array of surrounding seismometers and GPS stations is now the best documented such dyke injection in the world.

1. Constraining 3-D crustal velocity structure.

Construction of a 3D crustal velocity model beneath central Iceland using ambient noise tomography was led by Robert Green (Green et al. 2016 in prep). The University of Cambridge deployed 8 broadband seismometers around Vatnajökull in summer 2013 and 2014 under FUTUREVOLC and combined this data with data from Icelandic Meteorological Office (IMO) seismometers and with data from 67 other Cambridge seismometers deployed with funds outside FUTUREVOLC.

This multi-network study analyses continuous broadband seismic data from a total of 253 (not all simultaneous) seismic sites across Iceland (see Figure 1.1). 166 stations are part of an ongoing deployment in central and east Iceland, operated by the University of Cambridge and University of Iceland, and this array is augmented by 48 permanent sites from the monitoring network of the Icelandic Meteorological Office (IMO). To supplement this, additional archive data from the HOTSPOT experiment of 1996-98 (Allen et al., 1999) were collated and reprocessed to extend coverage to the edges of Iceland. Data for all networks was supplemented with records from the permanent Global Seismic Network (GSN) station BORG. Figure 1.1 displays the valuable ray path constraints in central Iceland which were added by the instrumentation installed as part of FUTUREVOLC.

Figure 1.1 [left] Complete set of stations used in this study. [right] Ray paths between broadband seismometers for ambient noise tomography in central Iceland.

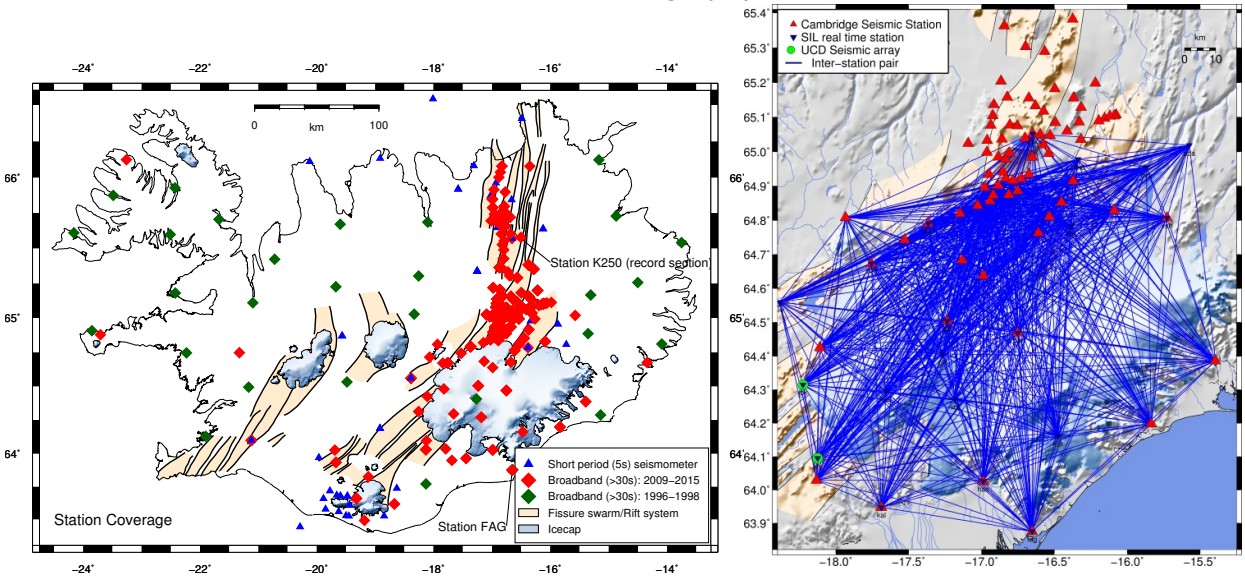

To prepare the continuous data, each day record was demeaned, detrended and tapered (to depress edge effects), before the instrument response is removed to displacement. Prior to the deconvolution, a high pass filter (tapering from 50 - 60 seconds) is applied to remove signals which are beyond the period range possible with station separations in Iceland. For data from short period instruments (Lennartz 5s and Güralp 40T) the high pass filter taper was 10 - 20 seconds. No additional low-cut filter is applied for (30 second response) semi-broadband sensors, in order to maximise the number of available paths with long period observations. Instead of low-cutting these continuous records at 30 - 40 seconds, a careful quality control procedure has been developed. This rejects

surface wave information at long periods if the signal quality is not sufficiently good in the resultant noise correlation functions.

The continuous displacement record is preprocessed in order to remove anything which is not the noise wave field; primarily earthquakes. The most important method to apply is temporal normalisation. This procedure reduces the effect of non-stationary noise sources and earthquakes on the cross correlation functions. We follow Bensen et al. (2007) and apply a running-absolute-mean normalisation. The method computes the running average of the absolute value of all samples in a sliding window along the waveform. The value at the centre of the window is then weighted by the inverse of that average.

Prepared noise time-series are cross correlated in the frequency domain to yield a two-sided Noise Correlation Function (correlation coefficient as a function of lag time). For all 11680 station pairs, day sections are correlated independently and then stacked. Increasing the number of days stacked improves the Rayleigh wave signal in the Noise Correlation Function (Figure 1.2). The final long term Noise Correlation Functions display very clear wave packets and a moveout on record sections showing a group velocity of 3 km/s, corresponding to that of a Rayleigh wave.

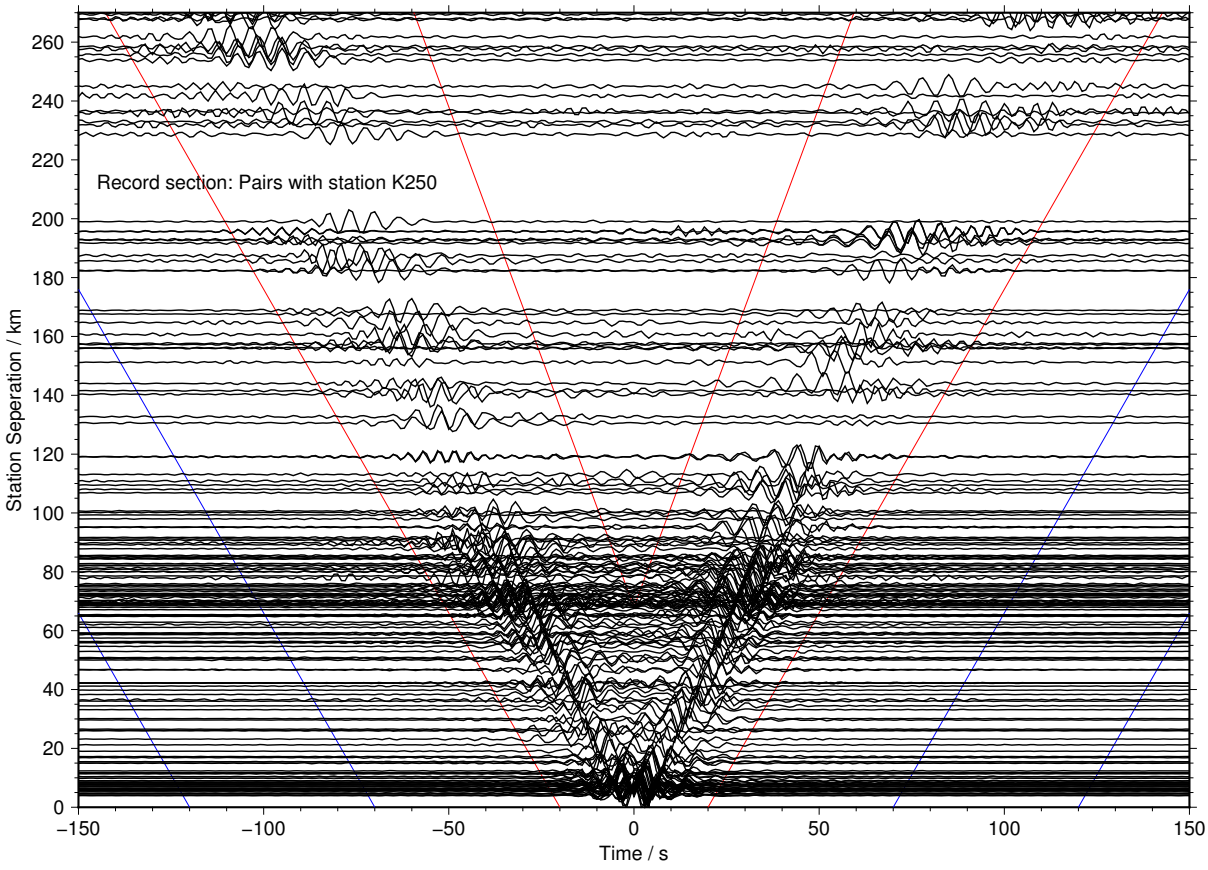

Fig. 1.2 Record Section of Noise Correlation Functions with station K250 (see Figure 1.1). Red lines show signal window and blue lines show noise window for signal-to-noise ratio calculations.

The signal-to-noise-ratio (SNR) of the emerging Rayleigh wave is determined between a signal window over the wave packet and a noise window trailing the

signal window by 50 seconds. The frequency dependence of the SNR is also a powerful parameter for assessing the quality of the signal emerging. A series of narrow bandpass filters are applied and the SNR measured using the peak in the signal window divided by the rms in the noise window. This is referred to as the spectral signal-to-noise-ratio and is displayed in Figure 1.3b. It is used in the quality control and data selection phase of the processing procedure.

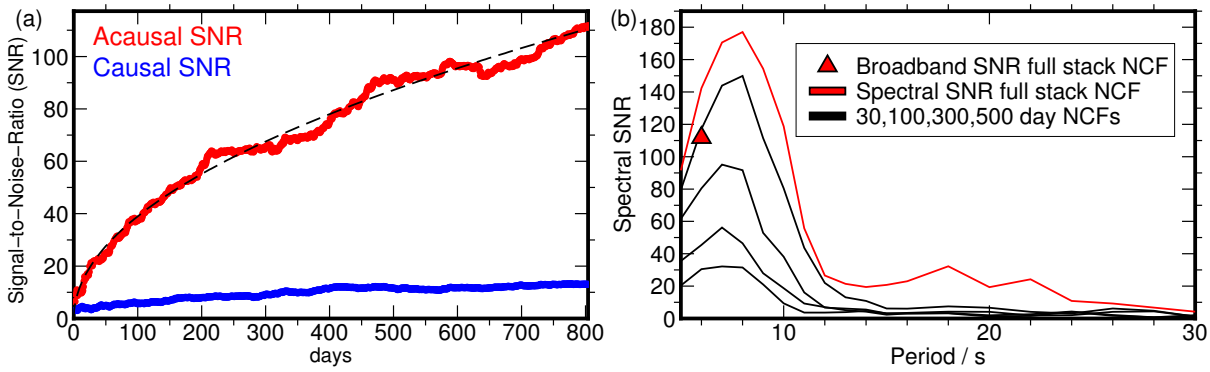

Fig. 1.3 Signal-to-Noise-Ratio emergence through stacking daily Noise Correlation Functions between stations FAG and K250. Broken line on (a) displays a square root relation.

Because energy close to the propagating azimuth is the dominant contributor to the NCF, we can use the asymmetric SNRs to estimate the directionality (Gerstoft et al., 2006). For each Rayleigh wave packet we calculate the broadband SNR and associate it with the station pair back-azimuth which represents the propagation direction of that surface wave. This is performed for casual and acausal Noise Correlation Functions for a large set of station pairs which have a distributed azimuthal sampling. We find that the most powerful surface waves arrive along a back azimuth from the south-west (160° – 280°). This direction corresponds to the main North Atlantic basin where the largest storms generate a powerful secondary microseism. There is a clear seasonal variation in the strength of the noise, with more powerful noise from the Atlantic ocean through the winter months.

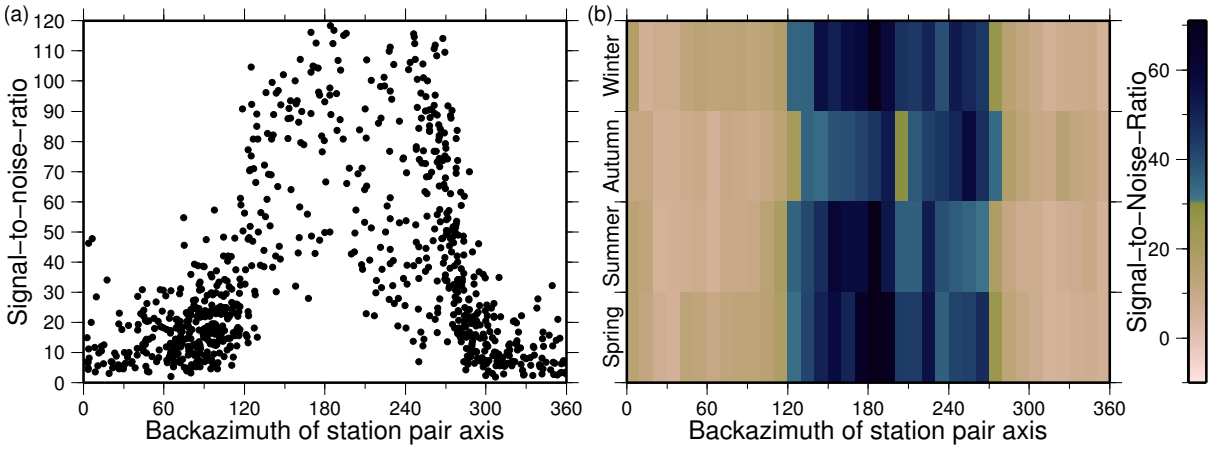

Fig. 1.4 Noise source directionality: Back azimuth variation of noise strength from signal-to-noise ratios. (a) SNR versus back azimuth of station pair for the full time stack Noise Correlation Function (NCF). (b) NCFs stacked in different seasons to display changes through the year.

Group Velocity Dispersion analysis

Rayleigh wave dispersion (group velocity variation as a function of frequency) is measured using Frequency Time Analysis (FTAN) (Dziewonski et al., 1969). The method used is based on the method of Levshin (1989) which has been modified for an automated application by Levshin and Ritzwoller (2001). This is necessary for use with large numbers of ambient noise observations, and its application has been demonstrated by Bensen et al. (2007). The automated frequency time analysis is applied to the available 11680 station pairings to measure the Rayleigh wave group velocity dispersion.

Quality Control and error analysis

To deal with the large data quantities we implement an automated quality control procedure and uncertainty analysis to ensure reliable velocity measurements. Noise conditions for the ambient noise velocity measurements are known to vary seasonally, and so assessing the temporal repeatability of these measurements through changing noise conditions is a significant indicator of their reliability. Any temporal variability in the measurements allows for the quantification of uncertainties and identification of outliers.

To do this we generate uncertainty correlation functions by stacking day cross-correlations in sliding 3 month windows with a 1 month shift. Each 3 month stack (or uncertainty correlation-function) is used to make a dispersion measurement with which to quantify uncertainty. These are used in the error analysis. The long term NCF stack of all available days is still used as the measurement waveform.

Several criteria are considered for the selection of a reliable dispersion measurement. First, we define a maximum Rayleigh wave period for each station pair, based on the inter-station separation. Observations are rejected if there are fewer than three complete wavelengths separating the two stations (Bensen et al., 2007). We then reject station pairs with a broadband signal-to-noise ratio less than 15 for the long term Noise Correlation Function. This reduces the available station pairings to 5669 paths.

The spectral signal-to-noise ratio is then used to limit the period band over which the Rayleigh wave is sufficiently well emerged in the narrow bandpass filters. If the signal-to-noise ratio at the separation defined maximum period is below 7, then the maximum observation period is reduced until the signal-to-noise ratio exceeds this value. This stage is vital for removing observations at longer periods where the frequency response or internal noise level of the seismometer means that the Rayleigh wave signal is not clearly defined. It allows the inclusion of data from a variety of instrument types because the long wavelength signals are rejected for data from short period seismometers.

Uncertainty stacks with a broadband signal-to-noise ratio greater than 10 are then used to quantify velocity uncertainties for the remaining observations. For each observation period, if there is a minimum of 4 uncertainty measurements then the error is defined as the standard deviation of all values. A minimum for the error is set as 0.01 km/s and in the absence of an uncertainty a default error of 0.05 km/s is assigned.

Ray Path Clustering

At periods between 8 and 20 seconds the dataset of available station-pair travel times is dominated by north-south ray paths. This is due to the high density of stations around the Askja Central Volcano linking with stations both on the north coast, and to the south of the Vatnajökull icecap. To negate the smearing effect which this causes on tomography maps we use a clustering methodology to reduce redundant paths. Stations more than 125 km from Askja are clustered with all stations in Askja. All dispersion curves within the cluster are then reduced to a single best fitting curve for each cluster. This averaging is performed by inverting all curves for the best fitting 1D shear wave velocity model. The model dispersion is used as this average. Errors for the cluster pair are estimated using the standard deviation of all dispersion curves in the cluster. Stations located closer, between 30 – 125 km from Askja are clustered with 4 spatially distributed subsets of Askja stations. Stations less than 30 km from Askja are clustered with 16 possible subsets of Askja stations. This process of removing redundant paths reduces the number of station pairs further to 2905.

Group Velocity Tomography

To generate group velocity maps the study region was parametrised with a 2-D mesh of triangular elements encompassing all stations. A node spacing of 0.1 degrees latitude and 0.2 degrees longitude is used across the majority of Iceland, though a finer grid is embedded within this, covering the Northern Volcanic Zone and the Vatnajökull ice cap. Here the high density of stations and ray paths merits a spacing of 0.05 degrees latitude and 0.1 degrees longitude. Tomographic maps at each period are generated following the method of Mitra (2004) and Mitra et al. (2006).

We construct Rayleigh wave group velocity maps at periods between 4 and 30 seconds. The input data amounts to 25919 group travel time paths. Ray path coverage is best at 6 – 8 seconds period, and is good between 5 seconds to 20 seconds. The inversion was performed using a range of values for the *a priori* slowness standard deviation at a reference distance of 10 km. This smoothing parameter was varied between 0.02 to 0.5 s/km. The choice of an *a priori* slowness of 0.06 s/km was made subjectively using overall misfit, physical reasonability and model error across the well sampled regions. The resulting model has a 0.1km/s error contour which is a good fit to the ray coverage, and is used to remove regions which are not constrained by the data.

Group velocity maps in Figure 1.5 are contoured at 0.1 km/s intervals. Low velocity regions in the map exhibit excellent correlation with the active rift systems of the plate boundary. Velocities are as much as 0.5 km/s slower at 10 seconds period than in the non volcanically active regions. Far from the active rifts the higher velocities in these regions imply cooler crust. The very lowest seismic velocities are centred beneath the western side of the Vatnajökull ice cap, where the thickest crust and centre of the mantle plume is believed to be positioned (Wolfe et al., 1997; Foulger et al., 2000; Foulger et al., 2001; Allen et al., 2002). The slow features distinctly correlate with the volcanic zones, and the margins of the velocity anomalies follow the edges of the rifts with remarkable consistency. The slow anomalies even delineate a linking branch between the Western Volcanic Zone and the Eastern Volcanic Zone near the Bárðarbunga-

Grimsvötn volcanic complex. The Höfsjökull-Kerlingarfjöll volcanic system beneath Hofsjökull glacier, and the Hveravellir and Prestahnjúkar volcanic systems beneath Langjökull glacier have clear low velocity anomalies associated with them. The Western Volcanic Zone exhibits less pronounced low velocities than the Eastern Volcanic Zone. Unfortunately, how far this feature extends down the Reykjanes Peninsula is limited by ray path coverage in this area.

Synthetic Recovery tests

Uncertainties in group velocity maps may arise from measurement errors and imperfect ray path coverage resulting in a poorly constrained inversion. Observational errors were quantified using the temporal repeatability of the dispersion measurement, and the effect of ray path coverage is assessed using a checkerboard recovery test. We performed a series of checkerboard tests of decreasing size to illustrate the resolution of the group velocity maps in this study. A synthetic model is parameterised with alternating blocks of high and low velocities of 4.0 and 2.5 km/s. Using the identical ray paths available for the real data at each period, we calculate the travel times for each path through the synthetic velocity model. The synthetic travel time data is then inverted using the same tomographic inversion. This is performed for block sizes of 40, 60, and 100 km (Figure 1.6).

For checker sizes of 60 km the structure is well recovered using the ray coverage between 5.0 – 14.0 seconds period, and at 15.0 seconds a small amount of NE-SW smearing is apparent. The velocity highs and lows are still resolved, albeit with a reduced amplitude which is typical for tomographic inversions. With smaller block sizes of 40 km, successful recovery is only achieved to 10–11 seconds and above this the features blur together. The velocity anomalies associated with the volcanic rift zones are greater than 60 km in lateral extent so they are likely to be reliably resolved by the data. Their correlation with the surface geology also acts as compelling support for the reliability of the structure.

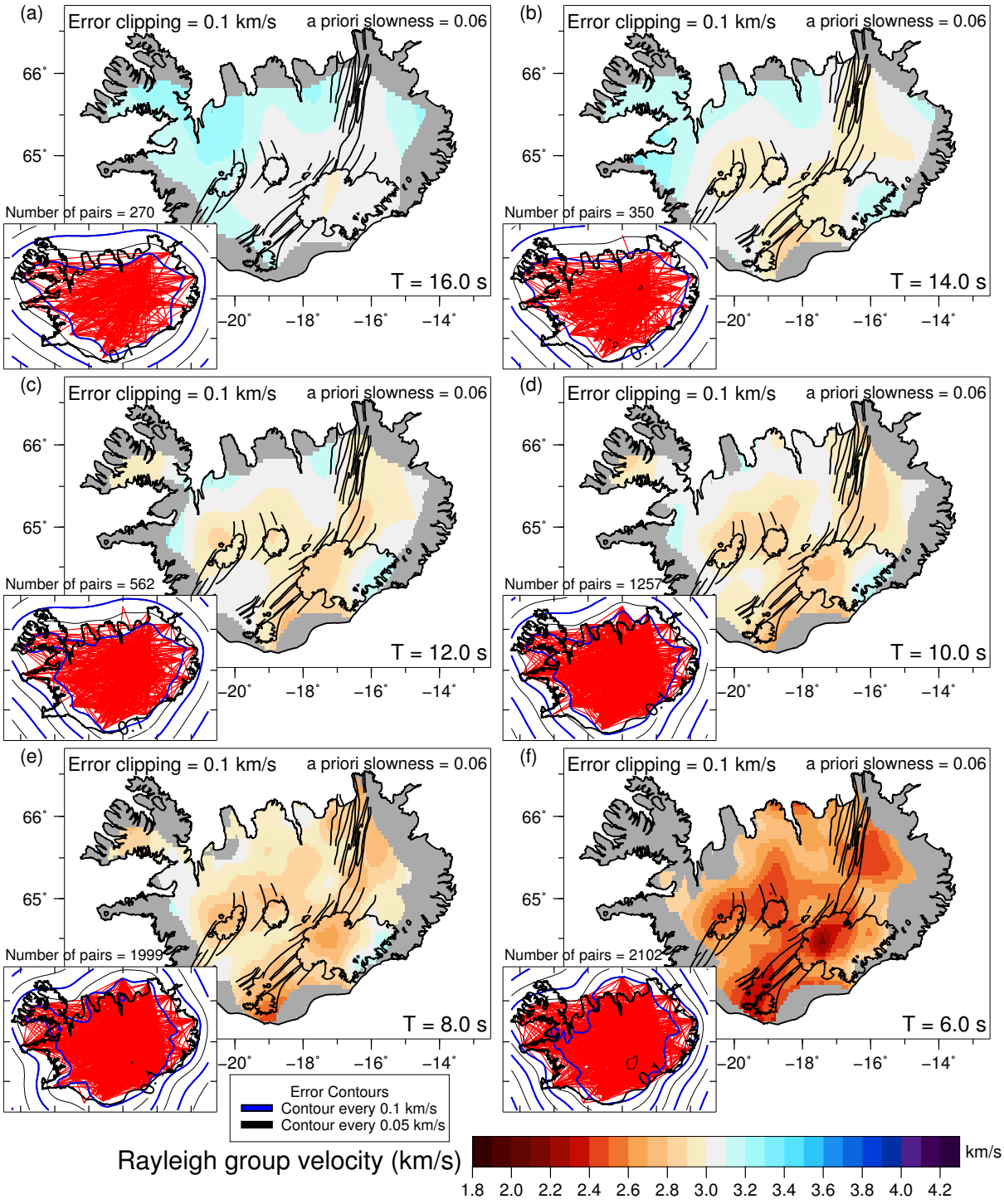

Fig. 1.5 Rayleigh Wave Group Velocity Maps between 16 s and 6 s period. Grey regions are unconstrained as the maps are clipped at the 0.1 km/s error contour. Black lines mark the rift systems and ice covered areas for reference. Small inset maps show the ray path distribution as red lines. Blue and black lines display error contours every 0.1 and 0.05 km/s. The damping parameter, a priori slowness is 0.06 for all maps.

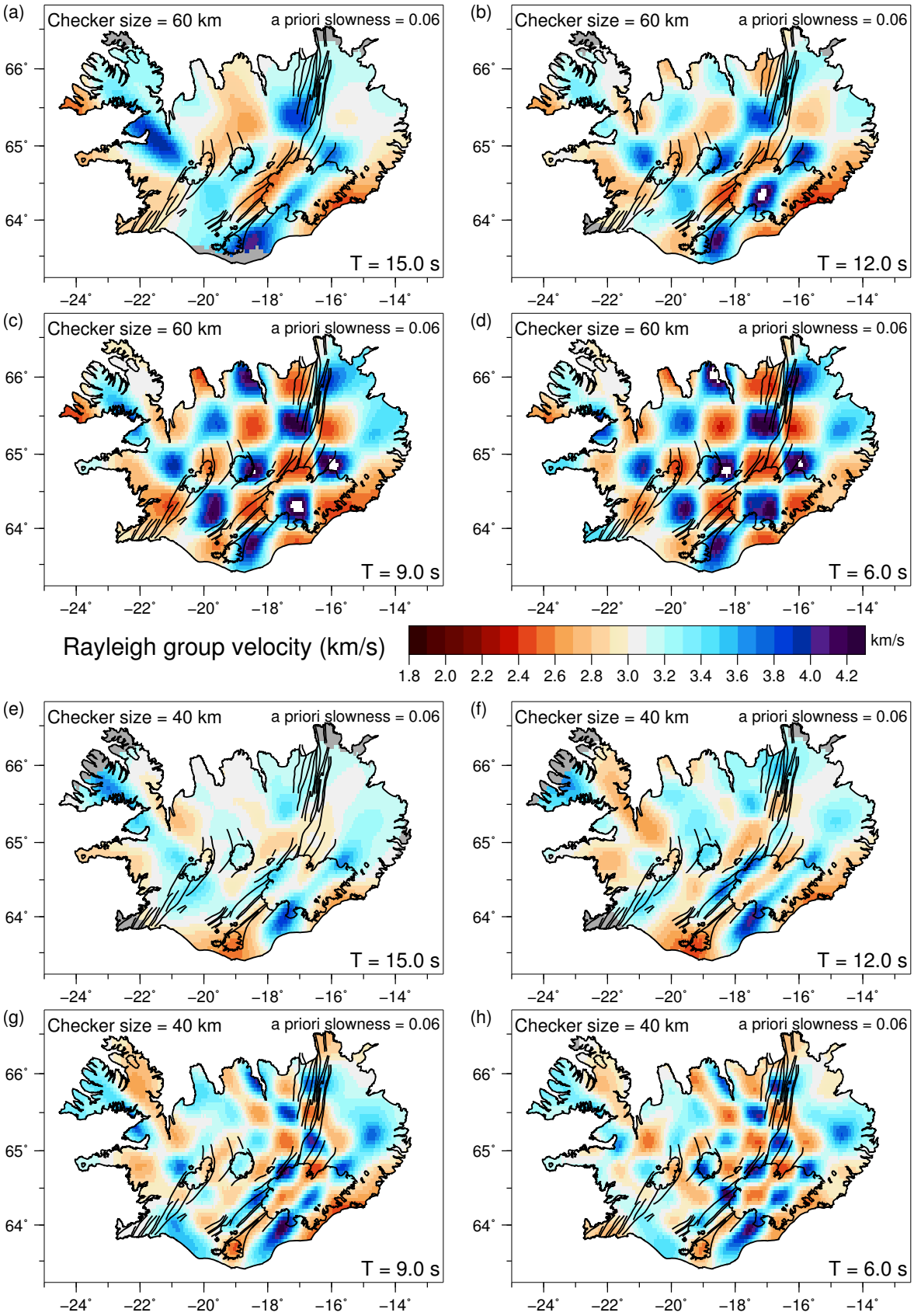

Fig. 1.6 Synthetic group velocity recovery maps for 15, 12, 9 and 6 s period, with identical ray coverage to the data inversions in Figure 1.5. Input checkerboard squares are 60 km (a-d) and 40 km (e-h).

Shear wave velocity structure

A shear wave velocity model across Iceland is obtained on grid cells in the regions of good group velocity constraint. Pseudo-dispersion curves are extracted from the group velocity maps using bicubic interpolation on a series of nodes at 0.05° latitude and 0.12° longitude spacing. The pseudo-dispersion curves are then grouped into 50 km wide cells to apply a regional smoothing. The dispersion data for each cell is inverted for a 1D shear velocity structure using *surf96* (Herrmann and Ammon, 2004).

A two-stage inversion procedure is used to achieve a good convergence of the model to the group velocity dispersion data. We parameterize a starting model of 1 km layers with a initial shear velocity of 3.9 km/s, compressional velocity of 6.8 km/s, and density of 2920 kg/m^3. The ratio of V_s to density and to V_p are kept constant during the inversion. In the first stage of the procedure we invert for a shear velocity structure which just fits the short period dispersion data between 4.5 and 11.0 seconds. The iterative inversion is allowed to run for 40 iterations, which is sufficient for the model to converge and achieve a good to the short period data. The shear velocity model from this first stage is then used as the starting model for the second stage where all the dispersion data is used in the inversion. The starting model in this procedure contains no preconceived structure and so any features of the inversion results are dictated by the data.

Shear velocity structures are presented in Figure 1.7. A cross sectional model of the shear velocity structure is generated by inverting groups of pseudo-dispersion curves in bins along a nearby projection line. The pseudo-dispersion data from within 20 km of the cross sectional line is projected onto the section, and the nodes are grouped into 20 km long bins along the cross section. The dispersion data is then inverted using the same two-stage procedure for a shear velocity structure in each bin. We show an along-rift cross section as well as three across-rift sections (Figure 1.8).

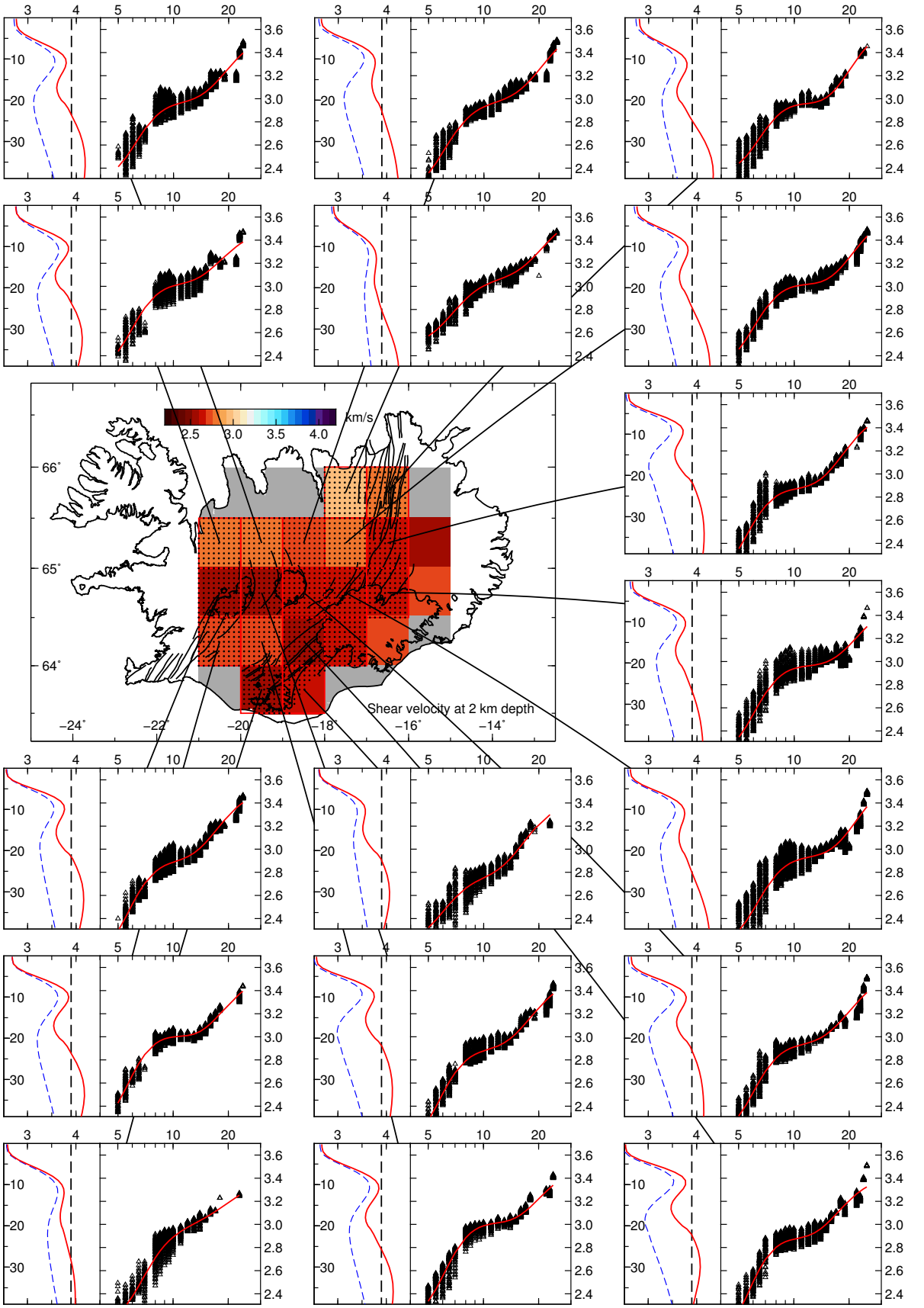

Fig. 1.7 Shear velocity structure on grid cells in the well constrained regions of the tomography maps. Each panel displays the dispersion curve on the right and shear velocity structure with depth on the left. Black line is initial model, blue line is model after first stage of inversion, red line is final Vs model.

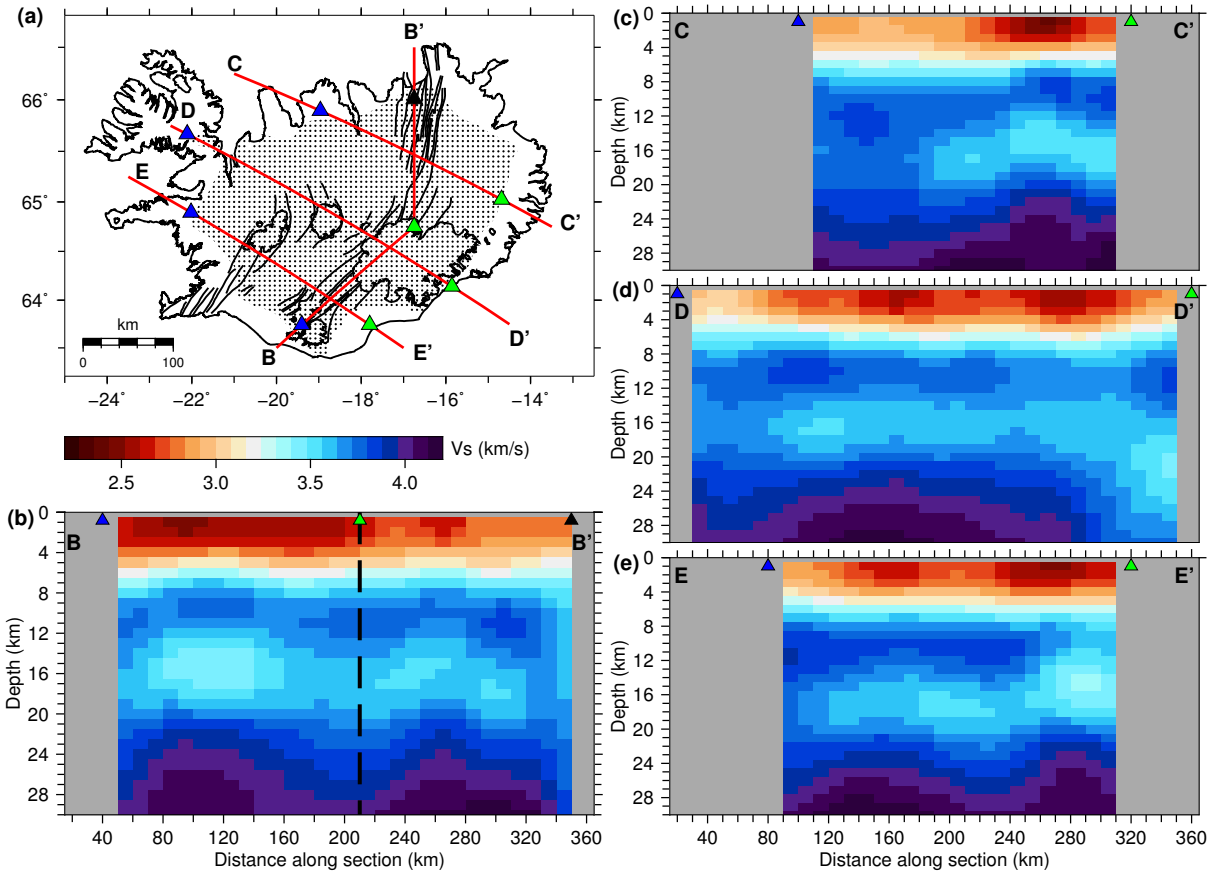

Fig. 1.8 Cross sections of shear wave velocity structure along rift (b) and across rift (c,d,e). (a) shows location of sections. Blue, green and black triangles are reference distance markers

Summary

We have resolved the 3D velocity structure across central Iceland using surface wave observations extracted from the ambient noise. Low group velocities are consistently associated with the volcanic rift zones across all Rayleigh wave periods. The non volcanically active regions on the other hand exhibit much faster wavespeeds.

The observed correlation between the shallow wavespeeds and the location of the volcanic rift zones is at a far superior resolution than previously observed. The shallow slow velocity anomaly even delineates a linking branch in central Iceland between the Eastern Volcanic Zone and the Hveravellir and Prestahnjúkar volcanic systems of the Western Volcanic Zone. Given that Iceland is compositionally rather homogeneous the velocity differences reflect variations in the thermal conditions, partial melt content and degree of fracturing. Within the rifts the slowest wave speeds are concentrated along the west of the Vatnajökull ice cap, and are centred below the Bárðarbunga-Grimsvötn volcanic complex. This is where the thickest crust and centre of the mantle plume is believed to be positioned (Wolfe et al., 1997; Foulger et al., 2000; Foulger et al., 2001; Allen et al., 2002).

The velocity structure which we have resolved shows a consistent low-velocity zone in the mid-crust between 14 – 20 km depth. This feature is observed across the entire model and has important implications for our understanding of

the Icelandic crust. Previous velocity models have traditionally been based on wide-angle refraction experiments with which it is difficult to observe low velocity zones. The 1-D velocity models used for earthquake location consequently currently contain only a gradational increase in seismic velocity.

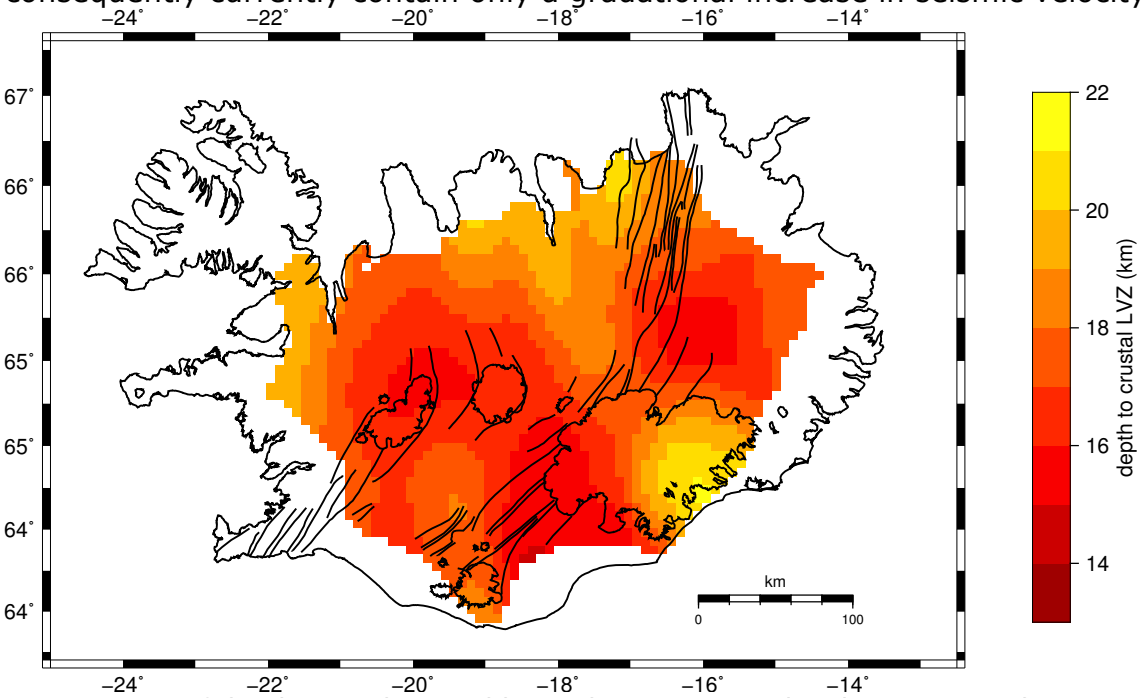

Fig. 1.9 Map of depth to mid-crustal low velocity zone in the shear wave velocity structure.

The resolution of a mid-crustal low-velocity zone is an important discovery, and the robustness of this observation is currently under further scrutiny. Additional receiver function analysis will be used to constrain how discontinuous this low-velocity zone is, as surface wave observations are limited by their ability to resolve smooth models.

2. Seismicity associated with melt movement

Our main work under the FutureVolc project has been constraining the seismicity associated with the Bárðarbunga - Holuhraun dyke intrusion. Melt moved 48 km laterally over a period of two weeks from the Bárðarbunga caldera to the eruption site at Holuhraun, just outside the Vatnajökull ice cap. We have located over 30,000 earthquakes during this melt propagation phase. The eight broadband seismometers deployed under FutureVolc funding were supplemented by 67 temporary deployments of 3-component seismometers by University of Cambridge under the leadership of Prof. Bob White plus some other stations deployed by IMO, UCD and BGS (Figure 1). The Cambridge group were also able to deploy at short notice four seismometers on the Vatnajökull ice cap and another 11 seismometers in the vicinity of the eruption site on Holuhraun. The last seismometer was deployed only two hours before the eruption began on 29th August 2014: these were so close to the eventual eruption site that two of them had to be removed at short notice before they were engulfed by lava.

Earthquakes were first located by the automated Cambridge Continuous Coalescence Microseismic Mapping program (Drew et al., 2013), and then subsequently refined both by manual picking of arrival phases and by NonLinLoc locations. Moment tensor solutions were then derived using a new Bayesian inversion method (Pugh et al., 2015). An important result from this was that the events could be explained by double-couple (DC) failure, with no requirement for non-DC components from, for example, volumetric changes. A second surprising result was that the failure mechanisms were all strike-slip, with the failure plane sub-parallel to the strike of the dyke, with the majority being left-lateral. This is explained in detail in Ágústsdóttir, Woods et al. (2016) (reproduced in Appendix 1), as failure at the dyke tip in the presence of magmatic fluids, moderated by the regional stress direction caused by plate spreading. Despite the large numbers of earthquakes caused by the melt propagation at 5−7 km beneath sea level, the total seismic moment release from the earthquakes is only 1% of the total geodetic moment release of the dyke. We conclude that most of the opening of the dyke is aseismic.

Full details of the methodology, results and interpretation are given in the paper in Appendix 1. The times and hypocentral locations of all 30,000 earthquakes during the dyke propagation phase are published in the Supplementary Materials of that paper and are also available from the FutureVolc web site.

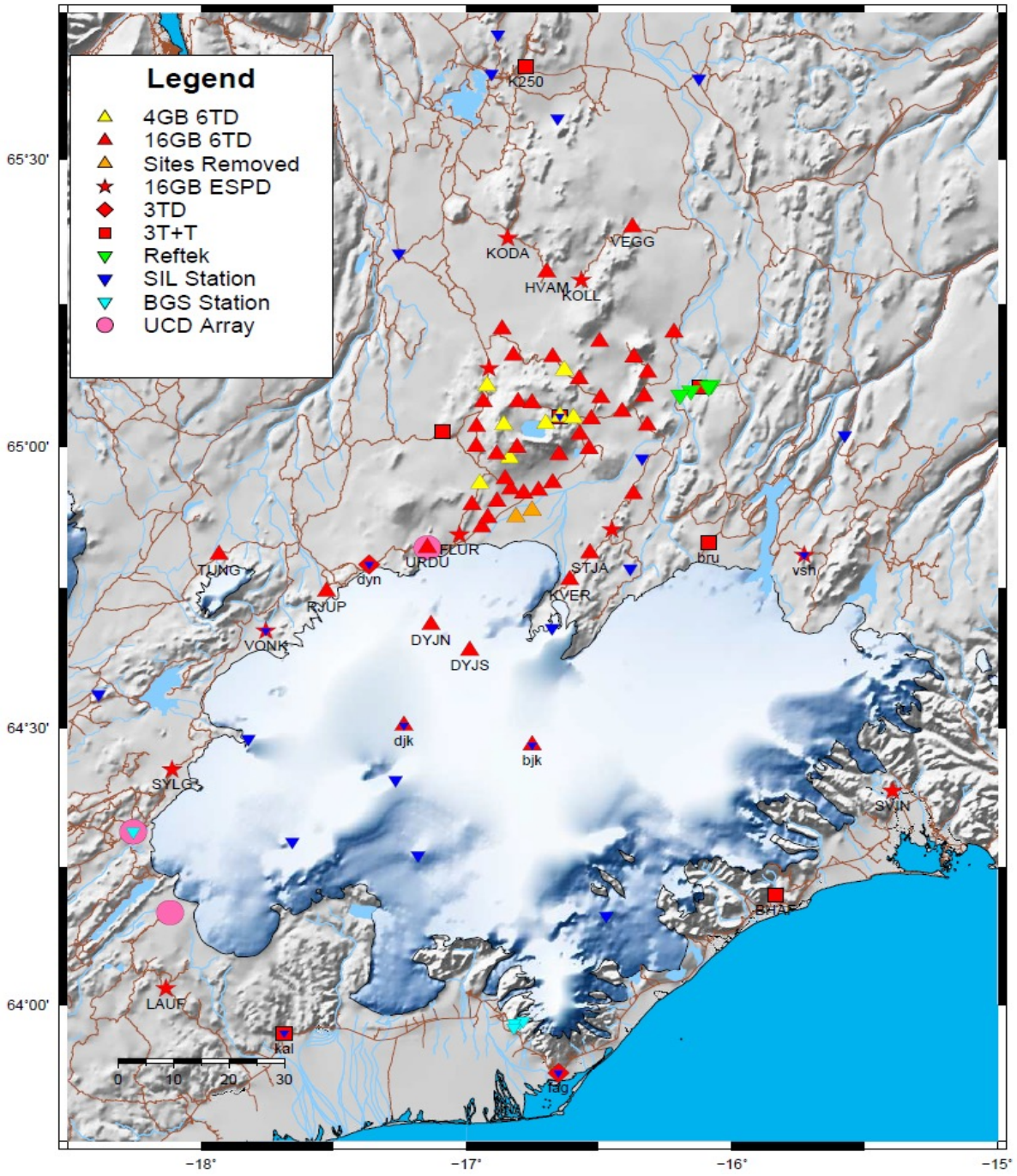

Figure 2.1. Seismometer deployments during the Holuhraun eruption 2014-15. Seismometer types are shown in the inset as well as stations operated by other institutions. All stations were deployed and operated by Cambridge University except those from the SIL network of IMO (dark blue triangles), some BGS stations (light blue triangles), and the arrays deployed by UCD (pink circles).

Publications

Ágústsdóttir, T., Woods, J., Greenfield, T., Green, R. G., White, R. S., Winder, T., Brandsdóttir, B., Steinthórsson, S. & Soosalu, H. (2016). Strike-slip faulting during the 2014 Bárðarbunga-Holuhraun dike Intrusion, central Iceland. *Geophysical Research Letters,* doi: 10.1002/2015GL067423

Drew, J., R. S. White, F. Tilmann, and J. Tarasewicz (2013), Coalescence microseismic mapping, *Geophys. J. Int.*, **195(3),** 1773–1785, doi:10.1093/gji/ggt331.

Green, R. G., Greenfield, T. & White, R. S. (2015). Triggered earthquakes suppressed by an evolving stress shadow from a propagating dyke, *Nature Geoscience,* **8**, 629–632, doi: 10.1038/NGEO2491

Pugh, D. (2015), *Bayesian Source Inversion of Microseismic Events*, PhD dissertation, University of Cambridge, 248 pp.

Sigmundsson, Freysteinn, Hooper, Andy, Hreinsdóttir, Sigrún, Vogfjord, Kristín, Ófeigsson, Benedikt, Heimisson, Elías Rafn, Dumont, Stéphanie, Parks, Michelle, Spaans, Karsten, Guðmundsson, Gunnar B., Drouin, Vincent, Árnadóttir, Thóra, Jónsdóttir, Kristín, Guðmundsson, Magnús Tumi, Högnadóttir, Thórdís, Friðriksdóttir, Hildur María, Hensch, Martin, Einarsson, Páll, Magnússon, Eyjólfur, Samsonov, Sergey, Brandsdóttir, Bryndís, White, Robert S., Ágústsdóttir, Thorbjörg, Greenfield, Timothy, Green, Robert G. et al. (2015). Segmented lateral dyke growth in a rifting event at Bárðarbunga volcanic system, Iceland, Nature, **517**, 191–195, doi:10.1038/nature14111

APPENDIX 1

Text of paper published as:

Ágústsdóttir, T., Woods, J., Greenfield, T., Green, R. G., White, R. S., Winder, T., Brandsdóttir, B., Steinthórsson, S. & Soosalu, H. (2016). Strike-slip faulting during the 2014 Bárðarbunga-Holuhraun dike Intrusion, central Iceland. *Geophysical Research Letters,* doi: 10.1002/2015GL067423

Title: Strike-slip Faulting During the 2014 Bárðarbunga-Holuhraun Dike Intrusion, Central Iceland.

Authors: Thorbjörg Ágústsdóttir[1,]*†, Jennifer Woods[1]†, Tim Greenfield[1], Robert G. Green[1], Robert S. White[1,2], Tom Winder[1], Bryndís Brandsdóttir[2], Sveinbjörn Steinthórsson[2], Heidi Soosalu[3]

Affiliations:

[1]Bullard Laboratories, Department of Earth Sciences, University of Cambridge, Madingley Road, Cambridge, CB3 0EZ, UK.

[2]Institute of Earth Sciences, University of Iceland, Askja, Sturlugata 7, 101 Reykjavík, Iceland.

[3]Geological Survey of Estonia, Kadaka tee 82, 12618 Tallinn, Estonia.

†The first two authors contributed equally to this paper.

*Correspondence to: ta354@cam.ac.uk

Key points:

Magma propagated 48 km laterally at 5–7 km below sea level prior to erupting, generating > 30,000 earthquakes

Seismicity arises from double-couple strike-slip failure orientated sub-parallel to the dike strike

Left-lateral fault motion is dominant to accommodate extension across the divergent plate boundary

Abstract:

Over a 13 day period magma propagated laterally from the sub-glacial Bárðarbunga volcano in the northern rift zone, Iceland. It created > 30,000 earthquakes at 5–7 km depth along a 48 km path before erupting on 29 August 2014. The seismicity, which tracked the dike propagation, advanced in short bursts at 0.3–4.7 km/h separated by pauses of up to 81 hours. During each surge forward, seismicity behind the dike tip dropped. Moment tensor solutions from the leading edge show exclusively left-lateral strike-slip faulting sub-parallel to the advancing dike tip, releasing accumulated strain deficit in the brittle layer of the rift zone. Behind the leading edge, both left- and right-lateral strike-slip earthquakes are observed. The lack of non double-couple earthquakes implies that the dike opening was aseismic.

Keywords:

Dike propagation, dike tip fracture, earthquake mechanisms, rifting, Bárðarbunga, Holuhraun

1. Introduction

Volcanic eruptions in rift zones are frequently preceded by lateral migration of a magma-filled dike, sometimes for many kilometers [*e.g. Rubin and Pollard*, 1988; *Rubin*, 1992; *Belachew et al.*, 2011]. Some of these dike intrusions freeze at depth while others breach the surface, resulting in a fissure eruption [e. g. *Björnsson and Saemundsson*, 1977; *Abdallah et al.*, 1979; *Hamling et al.*, 2009; *Wright et al.*, 2012]. Seismicity often accompanies propagation of the dike front as the magma forces its way forward [*Einarsson and Brandsdóttir*, 1978; *Brandsdóttir and Einarsson*, 1979; *Battaglia et al.*, 2005; *Morita et al.*, 2006; *Keir et al.*, 2009], commonly fed by a subsiding volcanic center [e.g. *Einarsson and Brandsdóttir*, 1978]. The extent of accompanying seismicity is variable, influenced strongly by the pre-existing stresses and material properties of the rift fabric [*Rubin and Gillard*, 1998; *Rivalta et al.*, 2015]. However, when seismicity is present the migrating earthquake swarm marks the tip of the intrusion [*Brandsdóttir and Einarsson*, 1979; *Grandin et al.*, 2011].

The Bárðarbunga volcanic system is made up of a sub-glacial central volcano with an ice-filled caldera and a transecting fissure swarm which extends 115 km SW (the Veiðivötn fissure swarm) and 55 km NNE (the Dyngjuháls fissure swarm) [*Jóhannesson and Saemundsson*, 1998; *Larsen et al.*, 2013; *Larsen and Gudmundsson*, 2015]. Episodic rifting within the fissure swarms of Icelandic volcanoes accommodates plate spreading along the

divergent plate boundary [*Tryggvason*, 1984; *Wright et al.*, 2012]. Gravity studies suggest that dense intrusions have previously radiated at depth from the Bárðarbunga central volcano [*Gudmundsson and Högnadóttir*, 2007].

In 2014 a dike propagated laterally 48 km from Bárðarbunga central volcano north-east along the Dynguháls fissure swarm. After 13 days propagation the dike erupted at Holuhraun, reoccupying old craters formed before the mid-nineteenth century by magma which also originated within the Bárðarbunga system [*Hartley and Thordarson*, 2013]. This study addresses the origin and extent of migrating seismicity accompanying the 2014 dike intrusion. The spatio-temporal resolution exceeds that of numerous previous observations of dike seismicity [*Passarelli et al., 2015; Rivalta et al., 2015 and references therein*]. We assess the relationship between the dike trajectory and seismicity, and construct precise fault plane solutions to investigate the failure mechanisms along the dike.

1.1. The 2014 Bárðarbunga-Holuhraun Dike Intrusion

On 16 August 2014 an unusual sequence of earthquakes began near the south-eastern rim of the ice-covered Bárðarbunga caldera. The earthquakes migrated rapidly 6 km south-eastwards, delineating a laterally propagating, radial dike, before turning 90° north-eastwards away from the caldera. Over the next twelve days the dike propagated episodically a further 42 km beneath the glacier and into the Holuhraun lava field. It advanced beyond the eventual eruption site by 2 km, making the total length of the dike 48 km (Figure 1, Movie S1). It was not until 29 August that the dike breached the surface, reoccupying the old Holuhraun craters. The initial fissure eruption lasted only 4 h. A further 40 h later, on 31 August, a sustained and larger fissure eruption began. It continued until 27 February 2015, erupting 1.6 km^3 of lava over an area of 84.1 km^2 [*Gíslason et al.*, 2015].

The dike propagation followed a pathway of minimum potential energy [*Heimisson et al.*, 2015; *Sigmundsson et al.*, 2015a]. Five large-scale segments can be identified, each distinguishable by a change in dike strike (Figures 1 and 2). The strike of the northernmost dike segment in the ice-free region is 025°, consistent with the regional rift fabric orientation of 025º [*Hjartardóttir et al.*, 2015a] but 11° clockwise from the normal to the plate spreading direction of 104°, extending at 18.5 mm/y [*DeMets et al.*, 2010]. Surface fracturing and graben formation accompanied the intrusion [*Hjartardóttir et al.*, 2015b]. Modeling of geodetic data shows that it was a vertically-extensive planar dike [*Green et al.*, 2015; *Sigmundsson et al.*, 2015a]. During the dike propagation Bárðarbunga caldera began to

subside and experienced over 50 M>3 earthquakes, suggesting a deflating magma reservoir beneath the caldera.

2. Seismic Data

A seismic network deployed by Cambridge University has been operated in Iceland since 2006 and expanded to surround Vatnajökull icecap in 2013. In August 2014 the network comprised 72 three-component broadband seismometers (Figures 1 and S1) that recorded the 2014 Bárðarbunga-Holuhraun dike propagation in detail. To complement the network, 14 stations from the national seismic network of the Icelandic Meteorological Office were used, as well as one British Geological Survey station and one University College Dublin station. The network provides good azimuthal coverage, with excellent sampling north of the ice cap. Coverage is less good to the south of the dike due to difficult field conditions on the icecap. The data used in this study covers the period from 16 to 31 August 2014, encompassing the whole dike intrusion and the onset of the two eruptions. All data were recorded at 100 Hz sample rate with a GPS time stamp.

More than 30,000 earthquakes (M_L 0.5–4) were automatically detected by Coalescence Microseismic Mapping [*Drew et al.*, 2013]. Accurate hypocenter locations were determined using NonLinLoc [*Lomax et al.*, 2000], with average location errors of 0.5 km laterally and 1.0 km in depth. We used a linear gradient velocity model for earthquake locations based on refraction experiments [*Pálmason*, 1971; *Gebrande et al.*, 1980; *Darbyshire et al.*, 1998] with a constant Vp/Vs ratio of 1.78, constrained by the Wadati-plots [*Wadati*, 1933] from manually picked phase arrival times along the whole dike (Figure S2, Table S1).

A manually constructed earthquake catalogue was created by refining earthquake arrival times for more than 500 events, producing 30,000 P-phase and 28,000 S-phase picks. Refined earthquakes were located with NonLinLoc to determine earthquake hypocenters with average errors of 0.5 km laterally and 0.9 km in depth (Figures 1, S2 and Table S3).

3. Bárðarbunga-Holuhraun Dike Seismicity

3.1. Seismicity Migration

During the intrusion new segments of the Bárðarbunga-Holuhraun dike were emplaced in propagation phases at speeds of 0.3–4.7 km/h, with seismicity focused around the dike tip. The advances were separated by periods where the migration stalled for up to 81 h. During periods of most rapid propagation, quiet zones occurred immediately behind the concentrated seismicity of the leading edge. The propagation phases are delineated by tight clusters in space and time of advancing earthquakes, highlighted by grey bands in Figure 2a. They last between 40 min and 13 h, with the longest continuous advance of 5.5 km made in 13 h. Large-scale dike segments were emplaced by episodic intrusion of many smaller segments with similar orientations. Each of the main segments became seismically quiet once a new segment had intruded beyond it, producing the step-like propagation of seismicity apparent in Figure 2a.

3.2. Seismicity Distribution

Throughout the dike emplacement, seismicity remained concentrated at 5–7 km below sea level, near the brittle-ductile boundary where differential stresses in this extensional area are greatest. The brittle-ductile boundary is mapped at about 7 km depth in the Askja volcanic system, located about 20 km along rift from the dike tip [*Key et al.*, 2011a,b *Green et al.*, 2014]. Sparse seismicity was observed in the uppermost four kilometers of crust at several sub-glacial locations (stars on Figure 1), but none near the eruption fissure, despite the dike breaching the surface. Persistent seismicity was observed at discrete locations along the dike, appearing as horizontal bands of seismicity on a distance-along-dike versus time plot (Figures 2a-b). A cluster at 37.5 km (64.80°N) occurred where the dike stalled for 14 h before surging forward. Another cluster is seen at 46 km (64.87°N), below the southern edge of the eruption fissure (Figures 2a–b).

3.3. Seismicity Rates and Moment Release

The majority of the seismic moment release accompanying intrusion of the Bárðarbunga-Holuhraun dike occurred during the rapid propagation phases (grey bands in Figure 2a). The largest increase in the moment release occurred simultaneously with the rapid advance of the dike on 24 August. Between propagation phases seismicity rates generally remained high but smaller magnitude earthquakes were observed. On several occasions the seismicity retreated or appeared to back-propagate, such as following the onset of the initial fissure eruption. In

this case the seismicity rate remained high but immediately retreated ~8 km along the dike, before migrating back to the eruption site over the subsequent 8 h. An instantaneous drop in seismicity rate along the entire dike was observed with the onset of the main eruption on 31 August (Figure 2).

3.4. Earthquake Source Mechanisms

In order to investigate the earthquake source mechanisms we concentrate on the 13 km of the dike nearest the eruption site (red box Figure 2a, beyond 64.78°N, emplaced from 24 August 2014). This northernmost segment of the dike has a strike of 025º and is where the seismic network provides the best azimuthal and spatial constraints. Lower hemisphere fault plane solutions and inversions of the full moment tensor were constructed using a Bayesian moment tensor solution program MTINV [*Pugh*, 2015]. Each event had a minimum distance to the nearest station of 1–7 km, a maximum azimuthal gap of 30°–50°, and an average of 53 P-phase polarities (Figure 3). Inversions for the full moment tensor revealed no significant volumetric component, despite the setting of an opening dike. All fault plane solutions are best described by double-couple failure. There is a surprising lack of normal faulting events, given this is an extensional rift setting (Figure S3). Instead, we find that the dominant failure mechanism is strike-slip. One nodal plane is consistently sub-parallel to the strike of the dike so we assume this to be the fault plane (Figures 4a–b). There is a significant range in the dike-perpendicular nodal plane orientations (Figure 3), strongly suggesting that they are not fault planes. It is therefore most likely that the fractures generated during the 48 km dike propagation are sub-parallel to the direction of travel.

The fault plane solutions constrain populations of left- and right-lateral strike-slip mechanisms with consistent fault planes (Figures 4a–b). The strike of the average left-lateral fault plane solution is 038° (Figure 4a, green on Figure S3b). This is a rotation of 13º clockwise from the strike of the dike and the regional rift orientation of ~025º [*Hjartardóttir et al.*, 2015a]. The right-lateral faulting observed occurs predominantly behind the leading edge, mainly in a cluster at 46 km (64.87°N) near the southern edge of the eruption fissure (red on Figure S3b). The strike of the average fault plane solution for this population is 017° (Figure 4b). The distribution of fault plane strikes is shown in the rose diagrams in Figures 4a-b.

3.5. Earthquake Fault Motion Categorization

A categorization method based on the consistency of the nodal planes (described above) was used to analyse the earthquake failure mechanisms in the northernmost dike

segment (Figure 2b). Two representative sets of stations from opposite polarity quadrants (dilatational and compressional) were selected with reliable, clear arrivals and stable locations on the focal sphere. Hence, plotting the earthquake arrival waveforms for both sets of 7 stations enabled quick differentiation between left- and right-lateral fault motion (Figure S4). Results from manually constructed fault plane solutions are consistent with the categorization (Figures 2b and S3b), allowing for the rapid failure mechanism analysis of ~9500 events.

The fault motion categorization shows that the principal failure mechanism along the dike is left-lateral strike-slip (85%, green on Figures 2b–c). Right-lateral strike-slip faulting is less common (15%, red on Figures 2b–c). The leading edge failure is exclusively left-lateral strike-slip. Right-lateral strike-slip failure only occurs after the leading edge of the dike has passed, persistently in a cluster at the southern end of the eruptive fissure, 1 km shallower than the majority of the seismicity (Figure 2c). Uncategorized earthquakes (grey on Figures 2b–c) are generally those with signal to noise ratios too low to confidently identify first motion polarities.

4. Discussion

As in other intrusions [*Brandsdóttir and Einarsson*, 1979; *Keir et al.*, 2009; *Belachew et al.*, 2011; *Grandin et al.*, 2011] the seismicity was confined to the region close to the front of the propagating dike, suggesting that the flow of magma is aseismic once a pathway has formed and remains open. The quiet zones observed immediately behind the leading edge during rapid propagation phases (grey bands on Figure 2b) may be due to stress shadowing [*Segall et al.*, 2013]. During the stalled phases a resupply of magma by lateral flow from Bárðarbunga volcano inflated the region behind the dike tip and allowed the pressure to build up sufficiently to drive the next advance forward [*Sigmundsson et al.*, 2015a]. The initial eruption on 29 August may have been short lived because it used up all the magma available in the dike and the pressure dropped. It then took two days for a consistent magma supply channel to form between the source and the fissures, before the start of the main, continuous eruption. Locations of persistent seismicity along the dike, behind the leading edge, may be due to an increase in local strength of the surrounding medium which required continual fracturing to maintain magma flow. Equally, they could arise from angular jogs in the dike,

such as at the southern end of the eruptive fissure where magma moves upward to the eruption fissure.

During emplacement, dike seismicity remained at 5–7 km depth. However, surface geodetic observations require most of the opening to be above 5 km depth [*Green et al.*, 2015; *Sigmundsson et al.*, 2015a]. The dike certainly extended shallower than the seismicity at the eruption fissure at Holuhraun. Small magma volumes may also have reached the surface at several other sub-glacial locations, especially where ice depressions formed at the surface (orange stars on Figure 1) [*Sigmundsson et al.*, 2015a]. We infer that the uppermost crust is so weak from the pervasive rift fabric that it fractured in tension and the dike inflated largely aseismically as magma was intruded and eventually froze. A similar lack of shallow seismicity was observed during the 1983 Kilauea dike intrusion [*Rubin et al.*, 1998]. Migrating magma in pre-fractured crust may propagate creating little brittle failure as shown by Taisne et al. (2011) where vertical magma propagation at Piton de la Fournaise is associated with fewer and smaller earthquakes than during lateral propagation phases.

Propagation rates vary along the Bárðarbunga-Holuhraun dike from 0.3-4.7 km/h. These speeds of lateral dike propagation, guided by pre-existing fractures, are comparable to those reported from other studies. Measured speeds of magma propagation at Piton de la Fournaise range from 0.7-2.9 km/h [*Battaglia et al.*, 2005; *Peltier et al.*, 2005] and 0.7-2.2 km/h for several rifting events during the 1975-1986 Krafla rifting episode, North Iceland, and the 2005-2010 rifting episode in Dabbahu, East African rift [*Wright et al.*, 2012]. Highest propagation rates are associated with short periods of rapid advance of the dike front on 16, 18 and 23 August.

The dike seismicity arises predominantly from double-couple strike-slip failure, with a minority of oblique normal faults (Figure 2b, S3b). The lack of non double-couple earthquakes implies that the opening was aseismic. This is supported by the two orders of magnitude difference between the geodetic moment and seismic moment release of the dike. Seismic moment reflects the brittle energy released by fracturing, whereas geodetic moment records the energy associated with the dike inflation. We calculate the seismic moment to be 1.8×10^{17} Nm and the geodetic moment to be 1.8×10^{19} Nm [*Green et al.*, 2015].

Seismicity along the leading edge of the dike arises exclusively from left-lateral strike-slip failure. These earthquakes exhibit greater seismic moment release than those behind the propagating front, where both left-lateral and right-lateral strike-slip failure is

observed. Left-lateral strike-slip failure is the dominant mechanism. This can be explained by the obliquity of the fault planes (038°) to the regional spreading axis (104°). Fault plane motion is preferentially left-lateral to accommodate extension across the divergent plate boundary. The strikes of the fault planes agree with theoretical models of dike tip failure which postulate fracturing oblique to the propagation direction. With a standard coefficient of friction of 0.6, fracturing would be expected ca. 30º to the dike strike, but high fluid pressures can cause greatly reduced fracture angles [*Rubin and Gillard*, 1998]. The high magmatic pressures at the dike tip are sufficient to reduce the angle of failure to 13º clockwise to the dike strike as observed (Figure 4d). Notably, no corresponding right-lateral events are observed along the leading edge on faults oriented 13º anticlockwise to the propagating dike tip. Any faults aligned in that direction would be almost exactly orthogonal to the spreading direction of 104º and may therefore fail aseismically in Mode I failure or at magnitudes smaller than our magnitude of completion (M_c 1.1). Nonetheless, small-scale faulting mapped at the surface close to the fissures shows both left-lateral and right-lateral failure clockwise and anticlockwise to the strike of the dike as predicted by our model [*Hjartardóttir et al.*, 2015b].

The path of the dike is governed by the pressure field produced by the overlying topographic load and the local stress field [*Sigmundsson et al.*, 2015a]. However, the influence of pre-existing weaknesses must also be considered. Fracture movements on pre-existing faults occur during rifting episodes, and the fracture density in fissure swarms in the northern rift zone gradually increases with time, indicating that dike intrusions tend to use the same pathways many times. The dike unquestionably reoccupied the old Holuhraun craters and the northernmost dike segment is parallel with the surrounding rift fabric [*Hjartardóttir et al.*, 2015a]. Hence, the dike is likely to have followed pre-existing weaknesses within the rift zone.

Throughout the propagation, eruption and cooling phases the seismicity remained concentrated at 5–7 km depth. We therefore infer that after the dike emplacement, an open pathway was formed and magma continued to flow along a conduit at ca. 6 km depth. The primary driving force for the magma flow through the 48 km long dike is likely to be the pressure head from the magma reservoir beneath Bárðarbunga. Effects of magma gas release are assumed to be minimal in the case of lateral sub-horizontal flow. It seems likely that the overburden pressure may have remained too high at the sub-glacial locations where ice depressions formed [*Sigmundsson et al.*, 2015a] for the pressure head available from the

magma reservoir to overcome. Instead, the magma migrated north until it reached a topographic low.

The Bárðarbunga caldera subsided 66 m from the beginning to the end of the eruption, accompanied by 79 M > 5 earthquakes [*Sigmundsson et al.*, 2015b]. The subsidence provides a measure of the available driving force for the magma flow. The average flow rate during the 6-month eruption was 100 m^3/s [*Gíslason et al.*, 2015] but at the beginning it was as high as 400 m^3/s [*Pedersen et al.*, 2015], dropping to zero at the end. A simple model of laminar flow through a tube, with an initial flow rate of 400 m^3/s, a driving force of 1.6 MPa (65 m thickness of magma with a density of 2500 kg/m^3) and a dynamic viscosity of 100 Pa s, requires a tube of 15 m diameter and a flow rate of 2.3 m/s (8.3 km/h). Using the average eruptive rate of 100 m^3/s and an average driving force of half the magma reservoir thickness (0.8 MPa), a similar size tube of 15.6 m diameter is required, but with a reduced flow rate of 0.8 m/s (2.9 km/h). This is within the bounds of the observed dike front propagation rates of 0.3–4.7 km/h, and suggests that once the flow path has been opened the lateral magma flow can continue unimpeded. The shape of the conduit need not be circular: equivalent flow rates are derived, for example, in rectangular conduits with a width of 7 m and a height of 100 m. Narrow, tall flow channels would fit the geodetic constraints on the extensional width of a few meters for a vertically extensive dike better than a circular channel.

5. Conclusions

The 2014 Bárðarbunga-Holuhraun dike propagated at 5–7 km below sea level, 48 km to the northeast from Bárðarbunga caldera, before erupting at Holuhraun. The propagation was episodic, advancing at velocities of 0.3–4.7 km/h. Seismicity remaining focused around the dike tip and at constrictions or jogs in the dike path. Detailed analysis of the northernmost dike segment reveals that the seismicity arises from double-couple strike-slip failure. Earthquakes along the leading edge are found to be exclusively left-lateral strike-slip failure, which is also the dominant mechanism overall. This preferential fault motion accommodates extension within the rift zone.

Acknowledgments:

Seismometers were borrowed from the Natural Environment Research Council (NERC) SEIS-UK (loans 968 and 1022), with funding by research grants from the NERC and the European Community's Seventh Framework Programme Grant No. 308377 (Project

FUTUREVOLC), and graduate studentships from the NERC and Shell. We thank Ágúst Þór Gunnlaugsson and others who assisted with fieldwork in Iceland and Nigel Woodcock for helpful discussions. M.T. Gudmundsson, H. Reynolds and Þ. Högnadóttir supplied ice cauldron coordinates. The Icelandic Meteorological Office, Chris Bean (University College Dublin) and the British Geological Survey kindly provided additional data from seismometers in north-east Iceland; data delivery from IMO seismic database 20151001/01. We thank the two anonymous reviewers for constructive comments. Hypocenter locations in Figure 1 are listed in Tables S2 and S3. Department of Earth Sciences, Cambridge contribution number ESC3539.

References :

Abdallah, A., V. Courtillot, M. Kasser, A.-Y. Le Dain, J.-C. Lépine, B. Robineau, J.-C. Ruegg, P. Tapponnier, and A. Tarantola (1979), Relevance of Afar seismicity and volcanism to the mechanics of accreting plate boundaries, *Nature*, *282*(5734), 17–23, doi:10.1038/282017a0.

Battaglia, J., V. Ferrazzini, T. Staudacher, K. Aki, and J.-L. Cheminée (2005), Pre-eruptive migration of earthquakes at the Piton de la Fournaise volcano (Réunion Island), *Geophys. J. Int.*, *161*(2), 549–558, doi:10.1029/2002JB002193.

Belachew, M., C. Ebinger, D. Coté, D. Keir, J. V Rowland, J. O. S. Hammond, and A. Ayele (2011), Comparison of dike intrusions in an incipient seafloor-spreading segment in Afar, Ethiopia: Seismicity perspectives, *J. Geophys. Res. Solid Earth*, *116*(B6), 2156–2202, doi:10.1029/2010JB007908.

Björnsson, A., and K. Saemundsson (1977), Current rifting episode in north Iceland, *Nature*, *266*, 318–323, doi:10.1029/JB090iB12p10151.

Brandsdóttir, B., and P. Einarsson (1979), Seismic activity associated with the September 1977 deflation of the Krafla central volcano in northeastern Iceland, *J. Volcanol. Geotherm. Res.*, *6*, 197–212.

Darbyshire, F. A., I. T. Bjarnason, R. S. White, and Ó. G. Flóvenz (1998), Crustal structure above the Iceland mantle plume imaged by the ICEMELT refraction profile, *Geophys. J. Int.*, *135*(3), 1131–1149.

DeMets, C., R. G. Gordon, and D. F. Argus (2010), Geologically current plate motions, *Geophys. J. Int.*, *181*(1), 1–80, doi:10.1111/j.1365-246X.2009.04491.x.

Drew, J., R. S. White, F. Tilmann, and J. Tarasewicz (2013), Coalescence microseismic mapping, *Geophys. J. Int.*, *195*(3), 1773–1785, doi:10.1093/gji/ggt331.

Einarsson, P., and B. Brandsdóttir (1978), Seismological evidence for lateral magma intrusion during the July 1978 deflation of the Krafla volcano in NE-Iceland, *J. Geophys., 47*, 160-165.

Einarsson, P., and K. Saemundsson (1987), *Í hlutarins eðli, Festschrift for Th. Sigurgeirsson*

(geological map), edited by T. Sigfússon, Menningarsjóður, Reykjavík.

Gebrande, H., H. Miller, and P. Einarsson (1980), Seismic structure of Iceland along the RRISP profile 1, *J. Geophys.*, *47*, 239–249.

Gíslason, S. R. et al. (2015), Environmental pressure from the 2014–15 eruption of Bárðarbunga volcano, Iceland, *Geochem. Perspect. Lett.*, *1*, 84–93, doi:10.7185/geochemlet.1509.

Grandin, R., E. Jacques, A. Nercessian, A. Ayele, C. Doubre, A. Socquet, D. Keir, M. Kassim, A. Lemarchand, and G. C. P. King (2011), Seismicity during lateral dike propagation: Insights from new data in the recent Manda Hararo–Dabbahu rifting episode (Afar, Ethiopia), *Geochem. Geophys. Geosyst.*, *12*(4), doi:10.1029/2010GC003434.

Green, R. G., R. S. White, and T. Greenfield (2014), Motion in the north Iceland volcanic rift zone accommodated by bookshelf faulting, *Nature Geosci.*, *7*(1), 29–33, doi:10.1038/ngeo2012.

Green, R. G., T. Greenfield, and R. S. White (2015), Triggered earthquake suppressed by an evolving stress shadow from a propagating dyke, *Nature Geosci.*, *8*, 629–632, doi:10.1038/ngeo2491

Gudmundsson, M. T., and T. Högnadóttir (2007), Volcanic systems and calderas in the Vatnajökull region, central Iceland: Constraints on crustal structure from gravity data, *J. Geodyn.*, *43*(1), 153–169, doi:10.1016/j.jog.2006.09.015.

Hamling, I. J., A. Ayele, L. Bennati, E. Calais, C. J. Ebinger, D. Keir, E. Lewi, T. J. Wright, and G. Yirgu (2009), Geodetic observations of the ongoing Dabbahu rifting episode: New dyke intrusions in 2006 and 2007, *Geophys. J. Int., 178* (2), 989–1003, doi:10.1111/j.1365-246X.2009.04163.x.

Hartley, M. E., and T. Thordarson (2013), The 1874-1876 volcano-tectonic episode at Askja, North Iceland: Lateral flow revisited, *Geochem. Geophys. Geosyst.*, *14*(7), 2286–2309, doi:10.1002/ggge.20151.

Heimisson, E. R., A. Hooper, and F. Sigmundsson (2015), Forecasting the path of a laterally propagating dike, *J. Geophys. Res. Solid Earth*, *120*(12), 8774-8792, doi:10.1002/2015JB012402.

Hjartardóttir, Á. R., P. Einarsson, S. Magnúsdóttir, Þ. Björnsdóttir, and B. Brandsdóttir (2015a), Fracture systems of the Northern Volcanic Rift Zone, Iceland: an onshore part of the Mid-Atlantic plate boundary, *Geol. Soc. London, Spec. Publ.*, *420*, 5825, doi:10.1144/SP420.1.

Hjartardóttir, Á. R., P. Einarsson, M. T. Gudmundsson, and T. Högnadóttir (2015b), Fracture movements and graben subsidence during the 2014 Bárðarbunga dike intrusion in Iceland, *J. Volcanol. Geotherm. Res.*, doi:10.1016/j.jvolgeores.2015.12.002.

Jóhannesson, H., and K. Saemundsson (1998), Jarðfræðikort af Íslandi, *Höggun (Geological Map of Iceland. Tectonics). Náttúrufræðistofun Íslands (Icelandic Inst. Nat. Hist.), Reykjavík*.

Keir, D. et al. (2009), Evidence for focused magmatic accretion at segment centers from lateral dike injections captured beneath the Red Sea rift in Afar, *Geology*, *37*(1), 59–62, doi:10.1130/G25147A.1.

Key, J., R. S. White, H. Soosalu, and S. S. Jakobsdóttir (2011a), Multiple melt injection along

a spreading segment at Askja, Iceland, *Geophys. Res. Lett.*, *38*(5), doi:10.1029/2010GL046264.

Key, J., R. S. White, H. Soosalu, and S. S. Jakobsdóttir (2011b), Correction to "Multiple melt injection along a spreading segment at Askja, Iceland," *Geophys. Res. Lett.*, *38*(10), doi:10.1029/2011GL047491.

Larsen, G., and M. T. Gudmundsson (2015), Catalogue of Icelandic Volcanoes - Bárðarbunga volcanic system, Available from: http://futurevolc.vedur.is/#

Larsen, G., M. T. Guðmundsson, P. Einarsson, and T. Thordarson (2013), *Náttúruvá á Íslandi - Eldgos og jarðskjálftar (Natural Hazards in Iceland – Eruptions and Earthquakes, in Icelandic)*, edited by S. Sólnes, F. Sigmundsson, and B. Bessason, Viðlagatrygging Íslands/Háskólaútgáfan, Reykjavík.

Lomax, A., J. Virieux, P. Volant, and C. Berge-Thierry (2000), Probabilistic Earthquake Location in 3D and Layered Models, in *Advances in Seismic Event Location*, vol. 18, edited by C. Thurber and N. Rabinowitz, pp. 101–134, Springer Netherlands.

Morita, Y., S. Nakao, and Y. Hayashi (2006), A quantitative approach to the dike intrusion process inferred from a joint analysis of geodetic and seismological data for the 1998 earthquake swarm off the east coast of Izu Peninsula, central Japan, *J. Geophys. Res. Solid Earth*, *111*(B6), doi:10.1029/2005JB003860.

Passarelli, L., E. Rivalta, S. Cesca, and Y. Aoki (2015), Stress changes, focal mechanisms, and earthquake scaling laws for the 2000 dike at Miyakejima (Japan), *J. Geophys. Res. Solid Earth*, *120*(B6), 4130–4145, doi:10.1002/2014JB011504.

Pálmason, G. (1971), *Crustal Structure of Iceland From Explosion Seismology*, Soc. Sci. Islandica, 187 pp.

Pedersen, G. B. M., A. Höskuldsson, M. S. Riishuus, I. Jónsdóttir, M. T. Gudmundsson, F. Sigmundsson, B. V Óskarsson, T. Dürig, V. Drouin, and C. Gallagher (2015), Nornahraun Lava Morphology and Emplacement: A New Terrestrial Analogue for Planetary Lava Flows, in *Lunar and Planet. Sci. Conf.*, vol. 46, p. 1845.

Peltier, A., V. Ferrazzini, T. Staudacher, and P. Bachèlery (2005), Imaging the dynamics of dyke propagation prior to the 2000–2003 flank eruptions at Piton de La Fournaise, Reunion Island, *Geophys. Res. Lett.*, *32*(22), L22302, doi:10.1029/2005GL023720.

Pugh, D. (2015), *Bayesian Source Inversion of Microseismic Events*, PhD thesis, University of Cambridge, 248 pp.

Rivalta, E., B. Taisne, A. P. Bunger, and R. F. Katz (2015), A review of mechanical models of dike propagation: Schools of thought, results and future directions, *Tectonophysics*, *638*, 1–42, doi:10.1016/j.tecto.2014.10.003.

Rubin, A. M. (1992), Dike-induced faulting and graben subsidence in volcanic rift zones, *J. Geophys. Res. Solid Earth*, *97*(B2), 1839–1858, doi:10.1029/91JB02170.

Rubin, A. M., and D. Gillard (1998), Dike-induced earthquakes: Theoretical considerations, *J. Geophys. Res. Solid Earth*, *103*(B5), 10017–10030, doi:10.1029/97JB03514.

Rubin, A. M., and D. D. Pollard (1988), Dike-induced faulting in rift zones of Iceland and Afar, *Geology*, *16*(5), 413-417, doi:10.1130/0091-7613(1988)016<0413:DIFIRZ>2.3.CO;2.

Rubin, A. M., D. Gillard, and J. L. Got (1998), A reinterpretation of seismicity associated with the January 1983 dike intrusion at Kilauea Volcano, Hawaii, *J. Geophys. Res. Solid*

Earth, *103*(B5), 10003–10015, doi:10.1029/97JB03513.

Segall, P., A. L. Llenos, S.-H. Yun, A. M. Bradley, and E. M. Syracuse (2013), Time-dependent dike propagation from joint inversion of seismicity and deformation data, *J. Geophys. Res. Solid Earth*, *118*(11), 5785–5804, doi:10.1002/2013JB010251.

Sigmundsson, F. et al. (2015a), Segmented lateral dyke growth in a rifting event at Bárðarbunga volcanic system, Iceland, *Nature*, *517*(7533), 191–195, doi:10.1038/nature14111.

Sigmundsson, F. et al. (2015b), Comparison of the Bardarbunga 2014-2015 rifting event, slow caldera collapse and major effusive eruption with the 1975-1984 Krafla and 2005-2010 Dabbahu, Afar, rifting episodes., T43H-05, AGU Fall Meeting 2015, San Francisco.

Taisne, B., F. Brenguier, N. M. Shapiro, and V. Ferrazzini (2011), Imaging the dynamics of magma propagation using radiated seismic intensity, *Geophys. Res. Lett.*, *38*, 2–6, doi:10.1029/2010GL046068.

Tryggvason, E. (1984), Widening of the Krafla fissure swarm during the 1975–1981 volcano-tectonic episode, *Bull. Volcanol.*, *47*(1), 47–69, doi:10.1007/BF01960540.

Wadati, K. (1933), On the travel time of earthquake waves, *Part II, Geophys. Mag.*, *7*, 101–111.

Wright, T. J. et al. (2012), Geophysical constraints on the dynamics of spreading centres from rifting episodes on land, *Nature Geosci.*, *5*(4), 242–250.

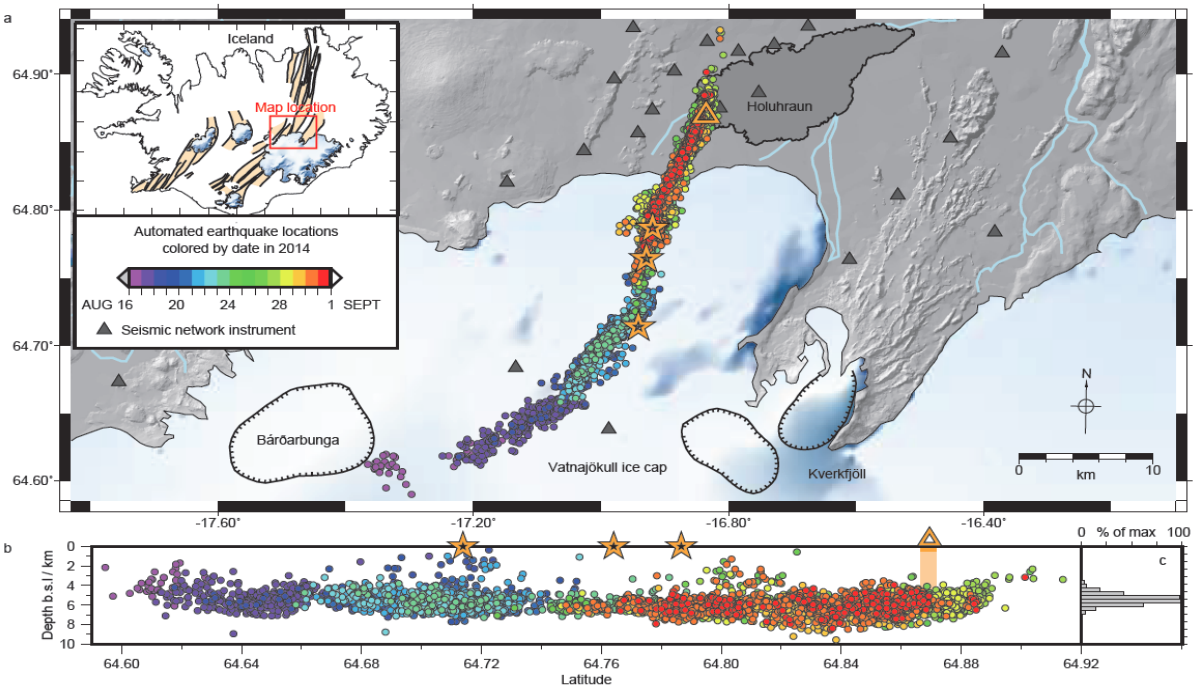

Figure 1. Seismicity produced by the propagating dike 16 - 31 August 2014, colored by date (see also Movie S1). (a) Earthquake locations in map view. Shaded topography in grey with glaciers in white. Ticked lines delineate central volcano calderas, triangles seismometers, orange triangle eruption site, stars depressions in the ice surface and dark shading new Holuhraun lava flow. Inset shows location on a simplified tectonic map of Iceland with volcanic systems shaded [*Einarsson and Saemundsson*, 1987]. (b) Cross section along dike. (c) Depth distribution of hypocenters.

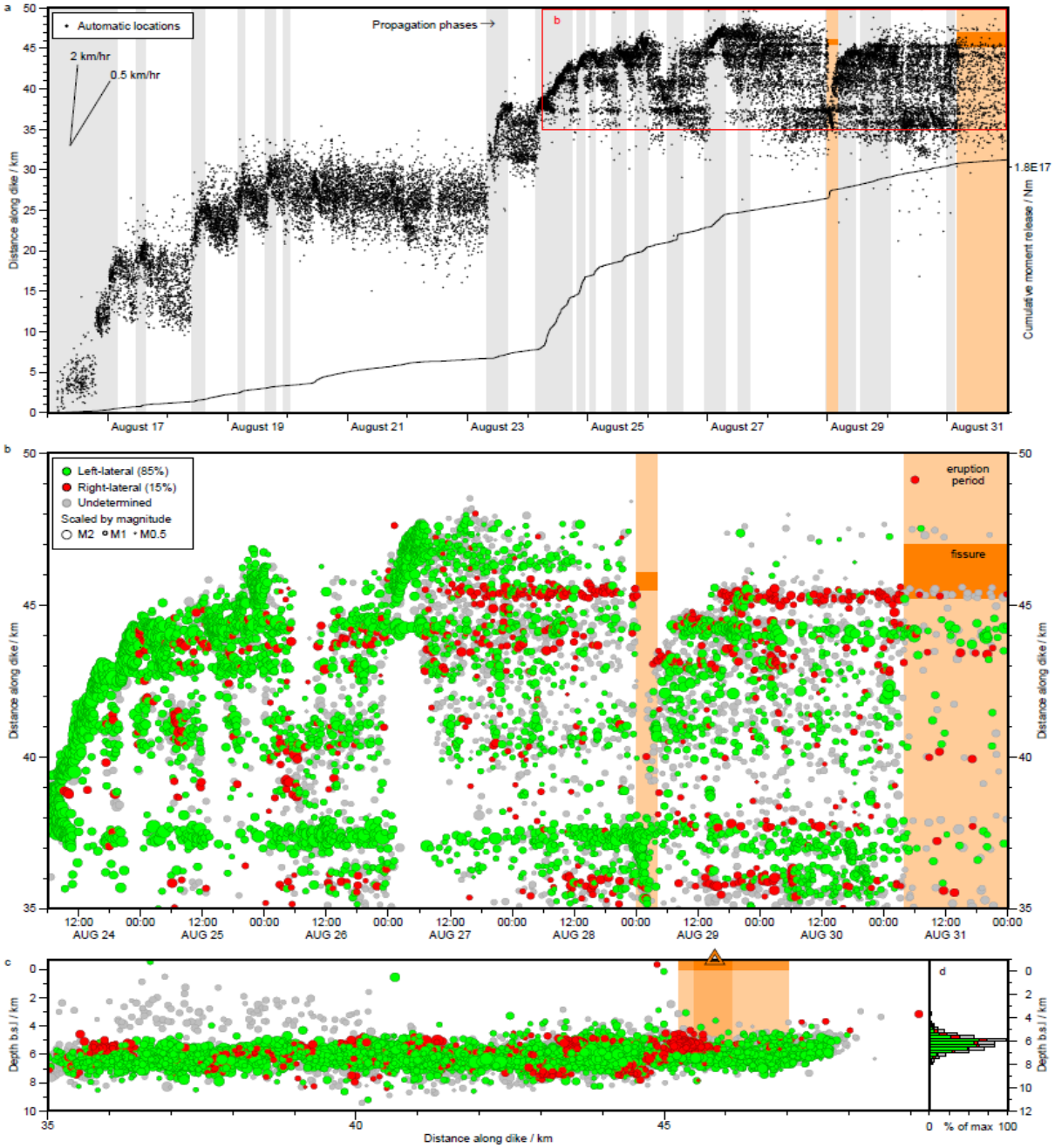

Figure 2. Propagation of seismicity through time with earthquake failure mechanisms. (a) Automated earthquake hypocenters (black dots) delineate segmented propagation of dike, plotted as distance-along-dike versus time. Propagation phases are shown in grey. Eruption periods are shown in peach, and fissure location in orange. Dike cumulative seismic moment release is shown by solid black line. (b) Inset from (a) with left-lateral (green), right-lateral (red) and undetermined (grey) fault mechanism categorizations (see section 3.5). Earthquakes scaled by magnitude. (c) Depth cross-section of (b), with main crater identified by orange triangle. (d) Distribution of depths in (c).

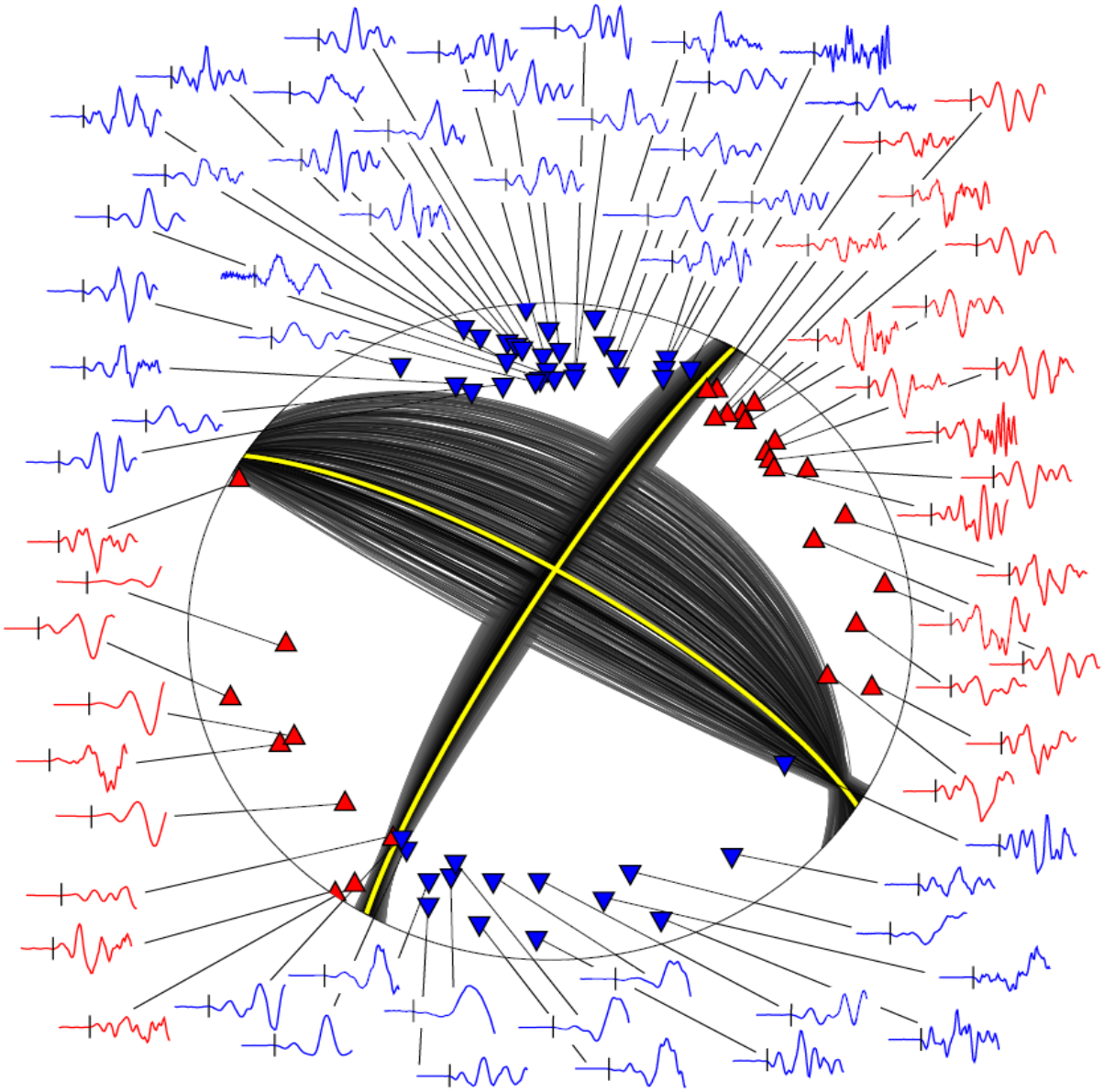

Figure 3. Example of fault plane solution with earthquake arrival waveforms. The fault plane solution is tightly constrained by polarity phase picks at 70 stations, each showing clear first motion polarity on vertical component. Each waveform is cut 0.25 s before first motion, 0.85 s in length and normalized to the same maximum amplitude. Red triangles represent compressional first motions, blue inverted triangles represent dilatational first motions. The range of possible fault plane solutions is given by the black lines, with the average fault plane solution highlighted in yellow. Location of earthquake is shown with a green star in Figure S3.

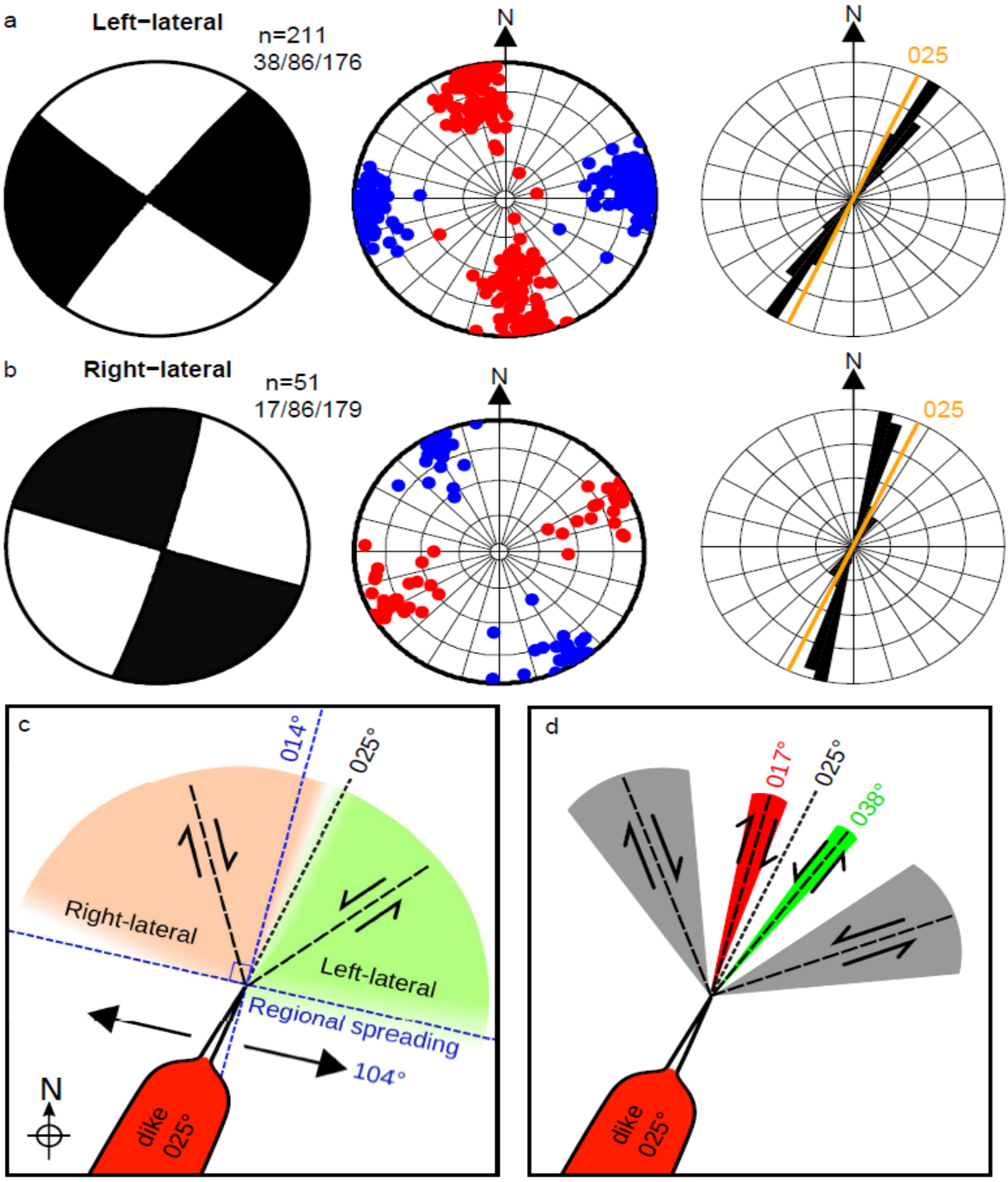

Figure 4. Fault plane solutions from northernmost segment of the dike shown in Figure 2b. Rows a–b, left to right: mean fault plane solution with strike/dip/rake marked; all P- (red) and T- (blue) axes; rose diagram of fault plane strikes, with strike of northernmost dike segment in the ice-free region in orange. (a) Left-lateral strike-slip faults. (b) Right-lateral strike-slip faults. (c) Schematic diagram showing fault motion produced by interaction of strike of dike with rift spreading direction. (d) Schematic diagram of dike tip fracture angles. *Rubin and Gillard* [1998] theoretical angles given by grey range, observed angles given by colored range. Left-lateral failure in green and right-lateral failure in red.